JACS
JOURNAL OF THE AMERICAN CHEMICAL SOCIETY
Article
Cite This: J. Am. Chem. Soc. 2018, 140, 807−813
pubs.acs.org/JACS

Orbitally Matched Edge-Doping in Graphene Nanoribbons

Rebecca A. Durr,[†,¶] Danny Haberer,[†,¶] Yea-Lee Lee,[‡,§,¶] Raymond Blackwell,[†] Alin Miksi Kalayjian,[†] Tomas Marangoni,[†] Jisoon Ihm,[§] Steven G. Louie,[*,‡,∥] and Felix R. Fischer[*,†,∥,⊥]

[†]Department of Chemistry, University of California Berkeley, Berkeley, California 94720, United States
[‡]Department of Physics, University of California Berkeley, Berkeley, California 94720, United States
[§]Department of Physics, Pohang University of Science and Technology, Pohang, Kyungbuk 37673, Korea
[∥]Materials Sciences Division, Lawrence Berkeley National Laboratory, Berkeley, California 94720, United States
[⊥]Kavli Energy NanoSciences Institute at the University of California Berkeley and the Lawrence Berkeley National Laboratory, Berkeley, California 94720, United States

Supporting Information

ABSTRACT: A series of trigonal planar N-, O-, and S-dopant atoms incorporated along the convex protrusion lining the edges of bottom-up synthesized chevron graphene nanoribbons (cGNRs) induce a characteristic shift in the energy of conduction and valence band edge states along with a significant reduction of the band gap of up to 0.3 eV per dopant atom per monomer. A combination of scanning probe spectroscopy and density functional theory calculations reveals that the direction and the magnitude of charge transfer between the dopant atoms and the cGNR backbone are dominated by inductive effects and follow the expected trend in electronegativity. The introduction of heteroatom dopants with trigonal planar geometry ensures an efficient overlap of a p-orbital lone-pair centered on the dopant atom with the extended π-system of the cGNR backbone effectively extending the conjugation length. Our work demonstrates a widely tunable method for band gap engineering of graphene nanostructures for advanced electronic applications.

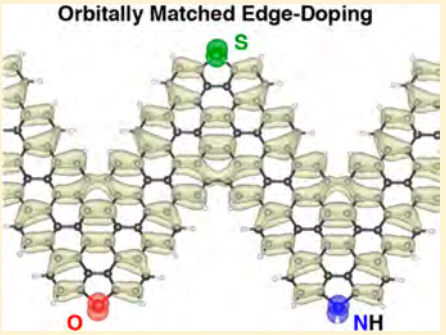

INTRODUCTION

Lateral quantum confinement of graphene has exposed a wealth of truly exotic physical and electronic properties in carbon-based nanomaterials. Graphene nanoribbons (GNRs) in particular have emerged as a privileged motif for applications in advanced electronics as they combine some of the most desirable intrinsic properties of graphene with the emergence of a highly tunable band gap. Minute variations in the width, the crystallographic symmetry, or the edge structure of GNRs can be translated into major shifts in the electronic band structure.[1−4] Deterministic bottom-up synthetic approaches based on judiciously designed molecular precursors have demonstrated an unprecedented atomic control over width,[5−8] edge topology,[9−13] and the placement of dopants[14−19] that is indispensable for the rational tuning of the electronic structure of GNRs.[20] The development, the fundamental exploration, and the mastery of these molecular engineering tools are critical steps toward the integration of functional GNRs into advanced electronic devices.[21−26]

A common strategy used to fine-tune the electronic structure of GNRs is the substitution of C atoms along the edges or along the backbone of GNRs with group 13 or 15 heteroatom dopants. Substitutional backbone-doping with B atoms demonstrated for $N = 7$ armchair GNRs (AGNRs) introduces deep-lying dopant states by forcing the empty p-orbital on B atoms into conjugation with the extended π-system of the GNR.[18,27] However, this backbone-doping strategy is limited to heteroatoms that can adopt the trigonal planar geometry required for the incorporation along the GNR backbone. A second approach used to alter the electronic structure of GNRs relies on replacing C−H groups along the ribbon edge. Nitrogen dopant atoms, for example, have been incorporated as part of pyridine or pyrimidine groups along the edges of chevron GNRs (cGNRs).[15−17] In these structures the lone-pairs of the N atoms come to rest in the plane of the ribbon, perpendicular to the extended π-system of the GNR backbone. Substitutional edge dopants alter the electronic structure of the GNR merely through inductive effects. This is reflected in the observation of a rigid shift of valence and conduction band edges with respect to the Fermi energy of the metal substrate, without any significant changes in the size of the band gap. Previous efforts aimed at incorporating edge-dopants in conjugation with the extended π-system of GNRs have led to defects and uncontrolled edge-reconstruction, yielding samples featuring heterogeneous doping patterns along the length of the ribbon.[14,19,28] Orbitally matched edge-doping merges both the inductive and the orbital overlap effects by placing heteroatom lone-pairs in conjugation with the extended π-system. This strategy not only provides a rational tool to control the relative energy of the band edge

Received: November 8, 2017
Published: December 15, 2017

DOI: 10.1021/jacs.7b11886
J. Am. Chem. Soc. 2018, 140, 807−813

states but also exerts control over the absolute size of the band gap.

Herein, we report the bottom-up synthesis of a series of atomically precise nitrogen-, oxygen-, and sulfur-doped cGNRs. The placement of trigonal planar heteroatom dopants at defined positions along the convex protrusion lining the edges of cGNRs ensures the overlap of the heteroatom lone-pairs with the extended π-system. N-, O-, and S-dopant atoms were selected in this series for their varying degrees of electronegativity. Samples of edge-doped cGNRs were prepared in ultrahigh vacuum (UHV) on a Au(111) surface. Scanning tunneling microscopy (STM) as well as noncontact atomic force microscopy (nc-AFM) confirms the precise dopant incorporation along the GNR edges. Scanning tunneling spectroscopy (STS) reveals a narrowing of the band gap by ~0.2−0.3 eV per dopant atom per monomer unit when compared to unsubstituted cGNRs. A correlation of the electronic band structures of N-, O-, and S-doped cGNRs establishes rational and predictable structure−function relationships that are corroborated by density functional theory (DFT) calculations.

RESULTS AND DISCUSSION

The molecular precursors for N-, O-, and S-doped cGNRs **1a−c** were synthesized through a Diels−Alder cycloaddition reaction between 5,10-dibromo-1,3-diphenyl-2*H*-cyclopenta[*l*]-phenanthren-2-one (**2**) and the respective carbazole **3a**, dibenzofuran **3b**, or dibenzothiophene **3c** followed by cheletropic extrusion of carbon monoxide and rearomatization to form the triphenylene cores (Scheme 1). Pale yellow crystals of **1a−c** suitable for X-ray diffraction were grown by slow evaporation of saturated $CHCl_3$/MeOH (**1a,b**) or toluene (**1c**) solutions (Figure 1). In the crystal, the fused heterocyclic rings in **1a−c** adopt dihedral angles C(1)−C(2)−C(1′)−C(2′) ranging from 105.9°, 108.5°, to 75.5°. The barrier to rotation around the C(2)−C(1′) bond is restricted, and the unit cells of **1a−c** contain racemic mixtures of both the R_a and S_a atropisomers.

N-, O-, and S-doped cGNRs were fabricated by thermal deposition of a submonolayer of the respective molecular building blocks **1a−c** on a Au(111) surface held at 120 °C in UHV.[12,14] STM images recorded on the intermediate polymer chains emerging from the step-growth polymerization of **1a−c** show characteristic protrusions along the edges commensurate with the expected position of the fused heterocyclic wings (Supporting Information, Figure S1). The irregular edge-pattern observed in the topographical images is consistent with a random *co*-polymerization of both the R_a and S_a enantiomers on the metal surface. Gradual annealing (5 K min^{-1}) first induces the complete cyclodehydrogenation of the triphenylene cGNR backbone until at 400−450 °C the heterocyclic wings fuse to form the extended graphitic backbone of cGNRs. Low-temperature (4.5 K) STM images of N-, O-, and S-doped cGNRs show an apparent height of 0.16 nm and the characteristic periodicity of 1.7 nm (Figure 2A−C).[12] Statistical analysis on different samples of doped cGNR reveals an average length clustering around 10−15 nm, with some cGNRs exceeding 40 nm (Supporting Information, Figure S2). While these observed parameters are consistent with the reported structures of the parent unfunctionalized cGNRs, we observed significant differences in the apparent width of N-, O-, and S-doped cGNRs, 2.3 ± 0.1, 2.2 ± 0.1, and 2.4 ± 0.1 nm, respectively.[29,30] Since variances in the apparent width of edge-doped cGNRs could be attributed to changes in the local electronic structure or result from the cleavage of the dopant heteroatom itself during the thermal annealing process, we performed nc-AFM imaging with CO-modified tips.[31] nc-AFM images of N-, O-, and S-doped cGNRs unambiguously confirm the position of dopant heteroatoms at the apex of each of the convex protrusion along the cGNR edges (Figure 2D−F). An evaluation of large area nc-AFM scans of doped cGNRs and the corresponding STM images indicates that N- and O-doped cGNRs retain >99% of the expected dopant atoms along the edges. Samples of S-doped cGNR, instead, suffer from sporadic defects resulting from the random excision of S atoms during the cyclodehydrogenation step. Statistical analysis shows that 15−20% of S-dopants are lost during the thermal annealing process (Supporting Information, Figure S3). Contrast in the nc-AFM images attributed to the position of N- and S atoms appears brighter than the position of O-dopants in corresponding images of O-doped cGNRs

Scheme 1. Synthesis of Molecular Precursors 1a−c for N-, O-, and S-Doped cGNRs

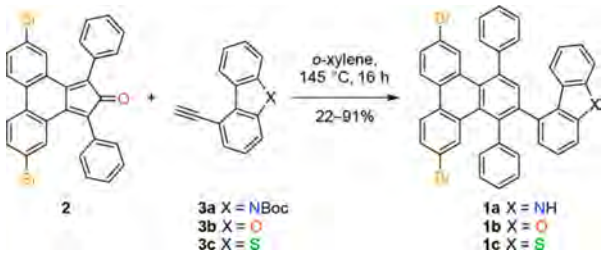

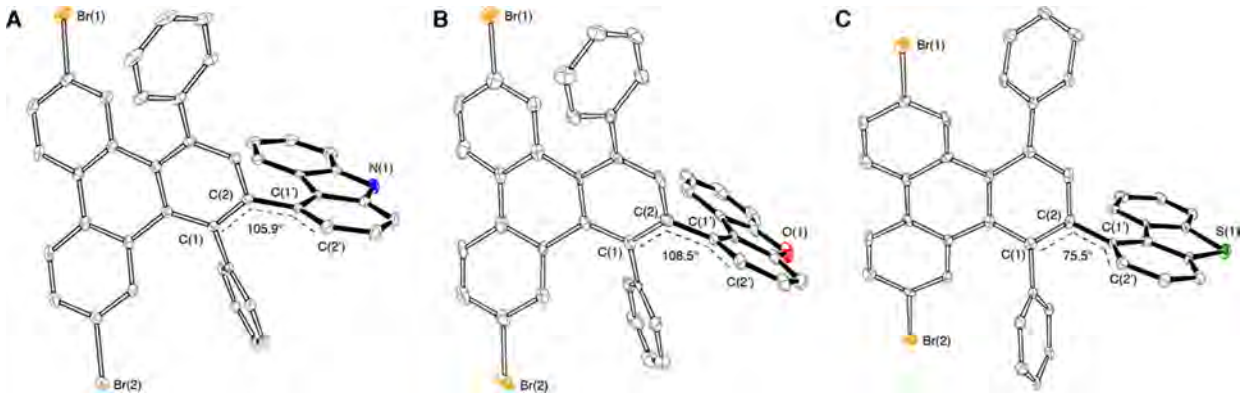

Figure 1. ORTEP representation of the molecular structures of the S_a atropisomers of (A) **1a**, (B) **1b**, and (C) **1c** found in the crystal structure. Thermal ellipsoids are drawn at the 50% probability level. Color coding: C (gray), Br (orange), N (blue), O (red), S (green). Hydrogen atoms and solvent molecules are omitted for clarity.

DOI: 10.1021/jacs.7b11886
J. Am. Chem. Soc. 2018, 140, 807−813

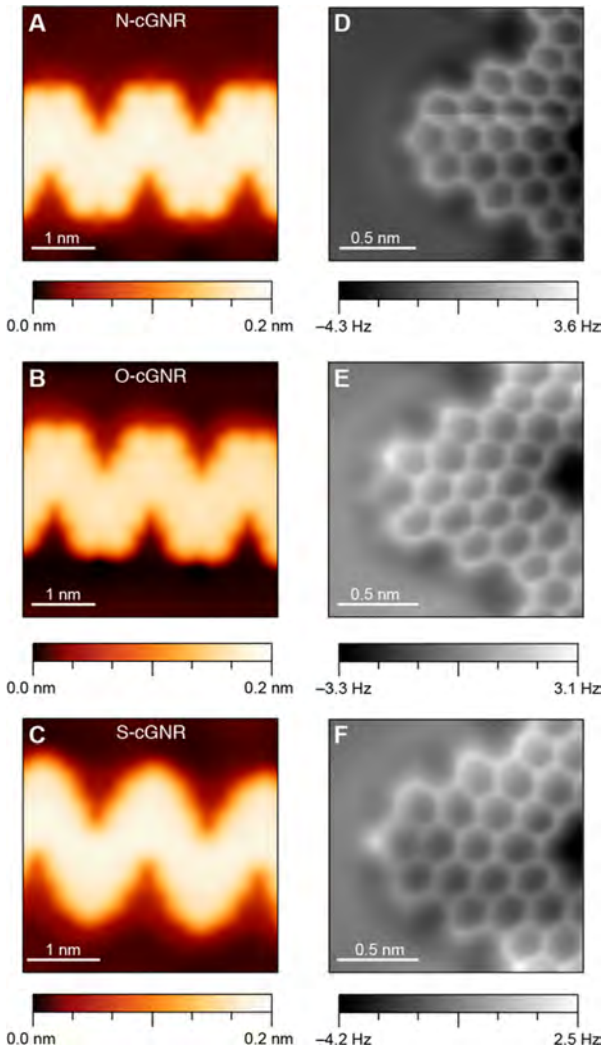

Figure 2. STM topographic image and nc-AFM frequency shift image of (A, D) N-doped cGNRs (V_{bias} = 10 mV, I_t = 40 pA), (B, E) O-doped cGNRs (V_{bias} = −1.1 V, I_t = 500 pA), and (C, F) S-doped cGNRs (V_{bias} = −0.75 V, I_t = 300 pA).

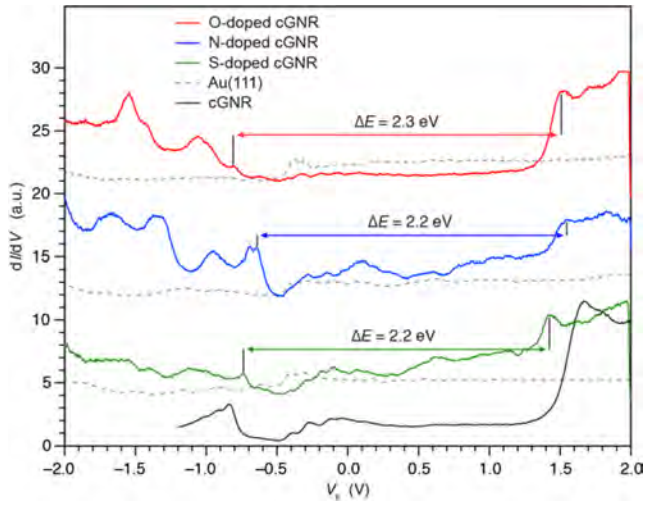

Figure 3. STM dI/dV point spectra of O-cGNR (red), N-cGNR (blue), S-cGNR (green), and representative Au(111) backgrounds (gray). Spectra were recorded at a position in the vicinity of the dopant atom along the GNR edge. Spectra are offset vertically (O-cGNR set point: V_{bias} = −1.1 V, I_t = 50 pA; S-cGNR set point: V_{bias} = 0.05 V, I_t = 20 pA; N-cGNR set point: V_{bias} = 0.05 V, I_t = 20 pA).

Table 1. Experimental and Theoretical (LDA) Band Gaps of N-, O-, and S-Doped cGNRs

	VB[a] edge	CB[b] edge	band gap
cGNR, exp.	−0.80	1.70	2.45 ± 0.05
cGNR, calcd	−3.36	−1.51	1.85
N-cGNR, exp.	−0.65 ± 0.02	1.55 ± 0.02	2.20 ± 0.05
N-cGNR, calcd	−2.91	−1.43	1.48
O-cGNR, exp.	−0.80 ± 0.02	1.50 ± 0.02	2.30 ± 0.05
O-cGNR, calcd	−3.19	−1.64	1.55
S-cGNR, exp.	−0.74 ± 0.02	1.46 ± 0.02	2.20 ± 0.05
S-cGNR, calcd	−3.08	−1.60	1.48

[a]Valence band. [b]Conduction band. In DFT-LDA, all band edge energies are chosen as the peak positions of the DOS, and the broadening of DOS is 0.06 eV. All energies are referenced to the vacuum level; all values reported in eV.

(Figure 2E). This superficial difference has in the past been attributed to the enhanced interaction between the terminal oxygen of the CO-modified tip and O atoms in molecular adsorbates.[32] Since nc-AFM imaging revealed no significant changes to the absolute width of N-, O-, and S-doped cGNRs, we conclude that the variations in apparent cGNR width observed by STM originate mainly from the modifications of the local electronic structure of the cGNRs by the dopant atoms.

We performed scanning tunneling spectroscopy (STS) on various samples of N-, O-, and S-doped cGNRs. Representative dI/dV point spectra acquired along the convex edge of cGNR close to the position of the heteroatom dopant are depicted in Figure 3. The experimental band edge energies and band gaps for N-, O-, and S-doped cGNR are summarized in Table 1. For this discussion, we operationally define the band gap as the peak-to-peak distance in the STS, and the band edge positions are similarly defined as the corresponding peak positions in the STS. The corresponding data for unfunctionalized cGNRs are provided as a reference.[33] When compared to pristine cGNRs, the introduction of O-dopant atoms leads to a significant shift of the conduction band (CB) edge to lower energies, while the valence band (VB) edge remains essentially unperturbed. This is reflected in a reduction (∼0.2 eV) of the band gap of O-doped cGNRs to 2.3 eV. The incorporation of S-dopant atoms in S-cGNR not only induces a significant shift of the CB edge to lower energies when compared to unsubstituted cGNRs and O-cGNR but also increases the energy of the VB by 0.1 eV when compared to the O-cGNR, leading to an overall reduction of the band gap to 2.2 eV. N-doping in N-cGNRs yields the largest observed increase in the VB energy within our doping series. The corresponding shift of the CB edge state is comparable to the O-doped cGNRs, leading to an overall reduction of the band gap of 2.2 eV, ∼0.3 eV smaller than the unsubstituted cGNRs. The relative energy of VB edge states follows the trend cGNR ≤ O-cGNR < S-cGNR < N-cGNR. The corresponding sequence for the CB band edge states is S-cGNR < O-cGNR < N-cGNR < cGNR.

We used dI/dV mapping to further explore the spatial distribution of VB and CB edge states in N-, O-, and S-doped cGNRs (Figure 4A−C, Supporting Information Figure S4). A common feature of all doped cGNRs is a confinement of the spatial distribution of the local density of states (LDOS) at the energy associated with the VB and the CB edge states to the geometric real-space edges of the ribbons.[16] In the VB edge state

DOI: 10.1021/jacs.7b11886
J. Am. Chem. Soc. 2018, 140, 807−813

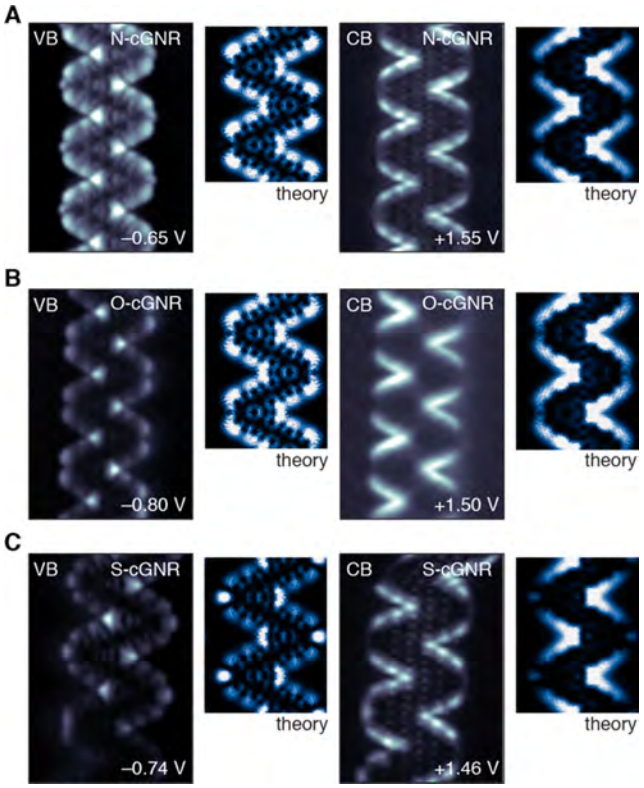

Figure 4. Experimental dI/dV spatial maps and calculated position dependence of the LDOS (or charge-density distribution) map of states with energy fixed at the valence band (VB) and the conduction band (CB) edges for (A) N-cGNRs (VB, I_t = 1.25 nA; CB, I_t = 10 nA), (B) O-cGNRs (VB, I_t = 300 pA; CB, I_t = 300 pA), and (C) S-cGNRs (VB, I_t = 1.5 nA; CB, I_t = 15 nA). Calculated lateral spatial distribution of LDOS at fixed energy is evaluated at a height of 4 Å above the doped cGNR plane.

dI/dV map of N- and S-doped cGNRs, bright protrusions corresponding to the position of the dopant heteroatoms can be observed. The analogous maps for O-doped cGNRs show a node at the expected position of the O atom. dI/dV maps of the CB edge states for N-, O-, and S-doped cGNRs are predominantly localized along the concave edges of the cGNRs and show a node at the position of the dopant heteroatom.

We performed DFT calculations within the local density approximation (LDA) to gain additional insight into the electronic structure of N-, O-, and S-doped cGNRs.[34] The introduction of dopant atoms at the apex of the convex edges of cGNRs significantly changes both the positions of band edge states and the energy band gaps. The DFT-LDA band gap of the heteroatom-doped cGNR series ranges from 1.4 to 1.6 eV, a decrease of ∼0.3−0.4 eV when compared the unsubstituted cGNR (Table 1). While calculations at the LDA level of theory for an isolated ribbon do not accurately account for the electron correlation effect to the self-energy of electron states nor the electron screening from the Au(111) substrate, previous studies show that the relative positions of band edge states and trends in the magnitude of the band gap can be faithfully reproduced.[35,36] This arises from a cancellation of errors: The enhancement of the band gap due to the self-energy correction is counteracted by the large metallic substrate screening, making the DFT Kohn−Sham gaps close to experiment by neglecting both. Thus, considering the three systems consistently within the same DFT-LDA framework, the reduction of the band gap in edge-doped cGNRs may be attributed to an extension of the π-conjugated network to include the p-orbital associated with the heteroatom dopant.[2,19,28] While the calculated density of states (DOS) of each isolated ribbon can only be referenced to the vacuum energy, we can still compare the relative movements of the positions of the VB and CB edges (Figure 5) with

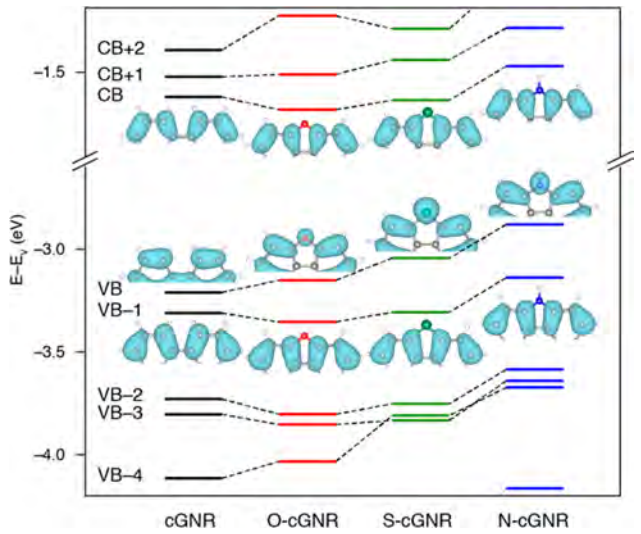

Figure 5. Calculated energy levels at the Γ point of unsubstituted cGNR (black), O-cGNR (red), S-cGNR (green), and N-cGNR (blue) near the band gap. Energy is referenced to the vacuum energy E_V. The wave functions of each cGNR at the CB, VB, and VB−1 along the GNR edges are shown as insets. Color coding for the atoms: C (black), O (red), S (green), N (blue). Hydrogen atoms and solvent molecules are omitted for clarity.

different dopants. The position of the theoretically predicted energy of the VB edge states (as defined by the peak in the density of states) in heteroatom-doped cGNRs mirrors the experimental trend determined by STS (cGNR < O-cGNR < S-cGNR < N-cGNR). The relative positions calculated for the CB edge states however deviate from the experimentally observed trend (O-cGNR < S-cGNR ≤ cGNR < N-cGNR). Most striking is the apparent inversion of the order between O-cGNR and S-cGNRs. In an effort to account for the experimental differences in the electronic structure of doped cGNRs, we investigated possible effects induced by the interaction of the ribbon with the underlying Au(111) substrate by calculating the interaction between 9*H*-carbazole (**4**), dibenzofuran (**5**), and dibenzothiophene (**6**) (small-molecule models for the functional groups lining the edges of N-cGNR, O-cGNR, and S-cGNR, respectively) and a four-layer Au(111) substrate (Supporting Information, Figure S5). Analysis of the relaxed atomic structures of small-molecule model systems on the Au(111) substrate shows a strong interaction between the dibenzothiophene group and the underlying substrate that is absent in the dibenzofuran and 9*H*-carbazole model and is directly reflected in the shorter S−Au distance (2.59 Å) between the substrate and the dibenzothiophene when compared to the corresponding structure of dibenzofuran or 9*H*-carbazole (O−Au 3.04 Å and N−Au 3.11 Å, respectively). Calculations show that a significant electron transfer from the Au substrate to the dibenzothiophene lowers the energy of the LUMO, leading to an inversion ($\mathbf{6}_{LUMO}$ < $\mathbf{5}_{LUMO}$ < $\mathbf{4}_{LUMO}$ on Au) of the trend observed in the gas phase ($\mathbf{5}_{LUMO}$ ≤ $\mathbf{6}_{LUMO}$ < $\mathbf{4}_{LUMO}$ gas phase, Supporting Information, Figure S6). The calculated

DOI: 10.1021/jacs.7b11886
J. Am. Chem. Soc. 2018, 140, 807−813

trend observed for the small-molecule model systems on Au(111) mirrors the experimentally observed changes in the relative alignment of the CBs in N-cGNRs, O-cGNRs, and S-cGNRs.

After accounting for the subtle changes induced by the underlying substrate, we can now rationalize the experimentally observed trends in the band shift of cGNRs upon introducing N-, O-, and S-dopant atoms along the edges. Two distinctive effects dominate changes in the band structure of edge-doped cGNRs: electron transfer between the GNR and the dopant atom and the expanded delocalization of the wave function to include the lone-pair p-orbitals at the site of the heteroatom. Löwdin charge analysis[34] suggests that each O- and S-dopant atom withdraws 0.17 and 0.12 electrons from the cGNR backbone. N atoms instead act as donors and contribute 0.11 electrons to the cGNR. This electron transfer generates a local potential gradient near cGNR edges, resulting in a downward shift of the overall band energies for O-cGNRs and S-cGNRs and an upward shift for N-cGNRs when compared to the parent unsubstituted ribbons. While our analysis does not account for higher-order many-body effects,[35] the relative energy level shifts should not change significantly as the electrostatic potential change due to the electron movement is expected to be much stronger than any induced changes in the self-energy correction. The observed band shift is supported by wave function analysis at the Γ point (Figure 5). The wave functions of doped cGNRs at CB, VB−1, VB−2, and VB−3 (VB−4 for S-cGNR) have the same character as unsubstituted cGNR, and their energy levels undergo a rigid shift to lower energies for O-cGNRs, a slightly smaller shift to lower energies for S-cGNR, and a shift to higher energies for N-cGNR. The wave functions of doped cGNRs at CB+2, CB+1, VB, and VB−4 (VB−3 for S-cGNR) show an overlap between the p-orbital lone-pair of the dopant atom and the extended π-system. The conjugation with the lone-pair leads to a reduction in the band gap (lowering the empty states and raising the occupied states relative to the midgap energy), leading to an upward shift of the occupied energy levels exceeding the potential gradient imparted by the electron transfer for the case of O- and S-doping. The alignment of electronic states near the Fermi level in orbitally matched edge-doped cGNRs is thus dictated by both the partial electron transfer between the dopant atoms and the cGNR (O- and S-dopants act as acceptors, while N-dopants are donors) and the effective conjugation of the extended π-system with the lone-pairs on the dopant atoms.

CONCLUSION

We herein report a deterministic strategy to tune the electronic band structure of bottom-up synthesized GNRs by introducing orbitally matched edge-dopant heteroatoms. Trigonal planar N-, O-, and S-dopant atoms incorporated along the convex protrusion lining the edges of cGNRs not only induce a characteristic shift in the energy of CB and VB edge states but lead to a significant reduction of the band gap of ∼0.3 eV for the fully doped case of one dopant atom per monomer. STS and DFT calculations reveal that the complex shifts in the electronic structure can be attributed to an inductive effect, a partial charge transfer between the cGNR backbone and the dopant atoms that correlates with the electronegativity of the dopant element, and an expansion of the effective conjugation length facilitated by the overlap of a p-orbital lone-pair on the trigonal planar dopant atoms with the extended π-system of the cGNR. Our modular and versatile doping strategy not only broadens the scope of accessible dopant atoms but also effectively blends the respective advantages of substitutional edge-doping and backbone-doping in a single step critical to the integration of functional GNRs into advanced electronic devices.

EXPERIMENTAL SECTION

Materials and General Methods. Unless otherwise stated, all manipulations of air- and/or moisture-sensitive compounds were carried out in oven-dried glassware under an atmosphere of N_2. All solvents and reagents were purchased from Alfa Aesar, Spectrum Chemicals, Acros Organics, TCI America, Matrix Scientific, and Sigma-Aldrich and were used as received unless otherwise noted. Organic solvents were dried by passing through a column of alumina. Flash column chromatography was performed on SiliCycle silica gel (particle size 40−63 μm). Thin-layer chromatography was performed using SiliCycle silica gel 60 Å F-254 precoated plates (0.25 mm thick) and visualized by UV absorption. All ^{1}H and $\{^1H\}^{13}$C NMR spectra were recorded on Bruker AV-600, AV-500, and AVQ-400 spectrometers and are referenced to residual solvent peaks ($CDCl_3$ ^{1}H NMR δ = 7.26 ppm, ^{13}C NMR δ = 77.16 ppm). High-resolution mass spectrometry (EI) was performed on an Autospec Permier (Waters) sector spectrometer in positive ionization mode. ESI mass spectrometry was performed on a Finnigan LTQFT (Thermo) spectrometer. STM, STS, and nc-AFM imaging were conducted in UHV ($p < 5^{-11}$ Torr) using an Omicron LT STM held at T = 4.5 K. STM images and dI/dV maps were recorded in constant current mode with a CO-functionalized W tip. STS point spectra were acquired at constant height (open feedback loop, tip set points indicated in figure captions) using the lock-in technique with f_{mod} = 455 Hz and V_{mod} = 10 mV. The W tip was prepared by repeated indentation into the Au(111) substrate prior to each measurement, and bare Au background spectra were recorded before and after measuring each doped cGNR. AFM measurements were recorded with a qPlus sensor[38] hosting a CO-functionalized W tip in frequency-modulation mode ($f_0 \approx$ 23 kHz; A = 60 pm) at constant height and V_{bias} = 0 V. STM and AFM images were processed using WSxM.[39] Theoretical calculations were performed within local density approximation (LDA) for each doped GNR species with slab geometries as implemented in the Quantum Espresso Package.[34] Norm conserving pseudopotentials with a planewave energy cutoff of 60 Ry were used,[37] and Monkhorst k-mesh was chosen as 6 × 1 × 1. The structure was fully relaxed until the force on each atom was smaller than 0.001 eV/Å. DFT calculations on small molecules on Au(111) were performed with ultrasoft pseudopotentials with energy cutoff of 40 Ry.[40] X-ray crystallography was performed on a MicroSTAR-H APEX II, using a microfocus rotating anode (Cu−K_α radiation), Kappa Geometry with DX (Enraf-Nonoius build) goniostat, a Bruker APEX II detector, Helios multilayer mirrors as the radiation monochromator, and Oxford Cryostream 700 held at 100 K (**1a**) or on an APEX II QUAZAR, using a Microfocus Sealed Source (Incoatec; Cu−K_α radiation), Kappa Geometry with DX (Bruker-AXS build) goniostat, a Bruker APEX II detector, QUAZAR multilayer mirrors as the radiation monochromator, and Oxford Cryostream 700 held at 100 K (**1b**,**c**). Crystallographic data were resolved with SHELXT, refined with SHELXL-2014, and visualized with ORTEP-32.

*Preparation of 4-(6,11-Dibromo-1,4-diphenyltriphenylen-2-yl)-9H-carbazole (**1a**).* A 50 mL Schlenk flask was charged with **3a** (300 mg, 1.04 mmol) and 5,10-dibromo-1,3-diphenyl-2*H*-cyclopenta-[*l*]phenanthren-2-one (560 mg, 1.04 mmol) in *o*-xylene (8 mL). The reaction mixture was heated to 148 °C and stirred for 17 h. The reaction mixture was cooled to 25 °C and concentrated on a rotary evaporator. Column chromatography (hexanes/CH_2Cl_2 1:0−7:3) yielded **1a** as a yellow solid (601 mg, 82%). ^{1}H NMR (400 MHz, 25 °C, $CDCl_3$) δ = 8.27 (dd, J = 8.8, 4.1 Hz, 2H), 8.09 (s, 1H), 7.88 (d, J = 2.0 Hz, 1H), 7.80 (s, 1H), 7.68 (d, J = 2.0 Hz, 1H), 7.57 (dd, J = 8.7, 2.0 Hz, 1H), 7.51 (dd, J = 8.7, 2.0 Hz, 3H), 7.40 (d, J = 8.0 Hz, 4H), 7.35−7.27 (m, 3H), 7.22 (s, 1H), 7.11 (d, J = 21.7 Hz, 3H), 7.03−6.81 (m, 4H), 6.73 (dd, J = 7.3, 0.9 Hz, 1H) ppm; ^{13}C NMR (151 MHz, 25 °C, $CDCl_3$) δ = 143.3, 141.0, 140.3, 139.6, 139.3, 138.8, 137.7, 135.9, 133.0, 132.8, 132.5, 131.8, 131.3, 131.0, 130.5, 129.8,

DOI: 10.1021/jacs.7b11886
J. Am. Chem. Soc. 2018, 140, 807−813

129.6, 129.5, 129.5, 129.3, 129.2, 128.2, 128.1, 127.6, 127.0, 125.6, 125.0, 124. 6, 124.5, 123.1, 122.1, 121.9, 121.8, 120.0 (2), 119.3, 110.3, 108.9 ppm; HRMS (EI) m/z: $[C_{42}H_{25}Br_2N]^+$, calcd for $[C_{42}H_{25}Br_2N]$ 703.0333; found 703.0335.

*Preparation of 1-(6,11-Dibromo-1,4-diphenyltriphenylen-2-yl)-dibenzofuran (**1b**).* A 50 mL round-bottom flask was charged with **3b-TMS** (20 mg, 0.08 mmol) in THF (5 mL) and MeOH (5 mL). K_2CO_3 (0.5 g) was added, and the reaction mixture was stirred for 2 h at 25 °C. The reaction was extracted with Et_2O (100 mL), and the combined organic layers were dried over $MgSO_4$ and concentrated on a rotary evaporator to yield **3b** (15 mg, 99%), which was used without further purification. A 10 mL Schlenk flask was charged with **3b** (15 mg, 0.08 mmol) and 5,10-dibromo-1,3-diphenyl-2*H*-cyclopenta[*l*]-phenanthren-2-one (42 mg, 0.08 mmol) in *o*-xylene (0.3 mL). The reaction mixture was heated to 145 °C and stirred for 16 h. The reaction mixture was cooled to 25 °C and concentrated on a rotary evaporator. Column chromatography (hexanes/CH_2Cl_2 3:1) to yielded **1b** as a colorless solid (12 mg, 22%). ^{1}H NMR (600 MHz, 25 °C, $CDCl_3$) δ = 8.29−8.23 (m, 2H), 7.86 (s, 1H), 7.78 (s, 1H), 7.67 (s, 1H), 7.58 (d, J = 8.7 Hz, 1H), 7.55−7.38 (m, 7H), 7.36 (t, J = 7.7 Hz, 1H), 7.20−7.08 (m, 4H), 7.03 (t, J = 7.5 Hz, 1H), 6.97−6.89 (m, 2H), 6.87 (d, J = 7.4 Hz, 1H) ppm; ^{13}C NMR (151 MHz, 25 °C, $CDCl_3$) δ = 156.2, 155.9, 143.1, 140.7, 138.9, 138.9, 137.7, 136.2, 132.9, 132.7, 132.3, 132.2, 131.7, 131.3, 131.1, 130.7, 129.9, 129.8, 129.6, 129.4, 129.3, 128.4, 127.7, 127.2, 126.9, 126.3, 124.8, 124.6, 124.5, 123.9, 122.5, 122.2, 122.0, 120.1, 120.0, 111.4, 109.9 ppm; HRMS (EI) m/z: $[C_{42}H_{24}OBr_2]^+$, calcd for $[C_{42}H_{24}OBr_2]$ 704.0168; found 704.0173.

*Preparation of 1-(6,11-Dibromo-1,4-diphenyltriphenylen-2-yl)-dibenzothiophene (**1c**).* A 10 mL Schlenk flask was charged with **3c** (20 mg, 0.10 mmol) and 5,10-dibromo-1,3-diphenyl-2*H*-cyclopenta-[*l*]phenanthren-2-one (52 mg, 0.10 mmol) in *o*-xylene (0.7 mL), and the reaction mixture was heated to 145 °C and stirred for 17 h. The reaction mixture was cooled to 25 °C and concentrated on a rotary evaporator. Column chromatography (hexane/EtOAc 19:1) yielded **1c** as a colorless solid (62.9 mg, 91%). ^{1}H NMR (600 MHz, 25 °C, $CDCl_3$) δ = 8.28 (dd, J = 8.8, 5.4 Hz, 2H), 7.88 (d, J = 2.0 Hz, 1H), 7.80 (d, J = 7.8 Hz, 1H), 7.75−7.70 (m, 2H), 7.69 (s, 1H), 7.58 (dd, J = 8.7, 2.0 Hz, 1H), 7.52 (dd, J = 8.7, 2.0 Hz, 1H), 7.50−7.38 (m, 5H), 7.34−7.26 (m, 3H), 7.15−7.04 (m, 4H), 7.00 (dd, J = 7.3, 1.0 Hz, 1H), 6.93−6.84 (m, 2H) ppm; ^{13}CNMR (151 MHz, 25 °C, $CDCl_3$) δ = 143.4, 140.9, 140.5, 139.9, 139.4, 138.0, 137.8, 135.8, 133.4, 133.2, 133.0, 132.7, 132.5, 131.9, 131.8, 131.2, 130.5, 130.2, 130.0, 129.9, 129.8, 129.6, 129.5, 128.7, 128.5, 128.0, 127.6, 127.4, 126.4, 125.6, 124.9, 124.8, 124.3, 122.8, 121.7, 120.4, 120.3 ppm; HRMS (EI) m/z: $[C_{42}H_{24}Br_2S]^+$, calcd for $[C_{42}H_{24}Br_2S]$ 719.9940; found 719.9945.

■ ASSOCIATED CONTENT

Supporting Information

The Supporting Information is available free of charge on the ACS Publications website at DOI: 10.1021/jacs.7b11886.

Figures S1−S6; methods and instrumentation; synthetic procedures for **3a**, 3b-TMS, **3c**; X-ray crystallographic data (Figures S7−S9 and Tables S1−S15); NMR spectra (Figures S10−S23) (PDF)

X-ray data for **1a** (CIF)

X-ray data for **1b** (CIF)

X-ray data for **1c** (CIF)

■ AUTHOR INFORMATION

Corresponding Authors

*ffischer@berkeley.edu

*sglouie@berkeley.edu

ORCID

Felix R. Fischer: 0000-0003-4723-3111

Author Contributions

‖These authors contributed equally.

Notes

The authors declare no competing financial interest.

■ ACKNOWLEDGMENTS

Research supported by the U.S. Department of Energy, Office of Science, Basic Energy Sciences, under Award no. DE-SC0010409 (design, synthesis, and characterization of molecules); the Center for Energy Efficient Electronics Science NSF Award 0939514 (STM and nc-AFM imaging, theory); SPM instrumentation is supported by the David and Lucile Packard Foundation for Science and Engineering; NSF Award DMR-1508412 and the Office of Naval Research MURI program Carbon-based Hierarchically Integrated Synthetic Electronics Award no. N00014-16-1-2921 (theory). Computational resources were provided by the DOE at Lawrence Berkeley National Laboratory's NERSC facility and the NSF through XSEDE resources at NICS. Berkeley NMR Facility is supported in part by NIH grant SRR023679A; Berkeley X-ray Facility is supported in part by NIH Shared Instrumentation Grant S10-RR027172. R.B. acknowledges support through a National Science Foundation Graduate Research Fellowship under grant no. DGE-1106400. The authors acknowledge Dr. Hasan Celik for support with NMR acquisition and Dr. Antonio DiPasquale and Stephen von Kugelgen for assistance with X-ray analysis.

■ REFERENCES

(1) Ezawa, M. *Phys. Rev. B: Condens. Matter Mater. Phys.* **2006**, *73*, 045432−045439.

(2) Son, Y. W.; Cohen, M. L.; Louie, S. G. *Phys. Rev. Lett.* **2006**, *97*, 216803.

(3) Barone, V.; Hod, O.; Scuseria, G. E. *Nano Lett.* **2006**, *6*, 2748−2754.

(4) Zhang, W.; Chen, Z.; Yang, B.; Wang, X.-Y.; Berger, R.; Narita, A.; Borin, G. B.; Ruffieux, P.; Fasel, R.; Feng, X.; Rader, H. J.; Müllen, K. *Anal. Chem.* **2017**, *89*, 7485−7492.

(5) Abdurakhmanova, N.; Amsharov, N.; Stepanow, S.; Jansen, M.; Kern, K.; Amsharov, K. *Carbon* **2014**, *77*, 1187−1190.

(6) Chen, Y.-C.; de Oteyza, D. G.; Pedramrazi, Z.; Chen, C.; Fischer, F. R.; Crommie, M. F. *ACS Nano* **2013**, *7*, 6123−6128.

(7) Kimouche, A.; Ervasti, M.; Drost, R.; Halonen, S.; Harju, A.; Joensuu, P. M.; Sainio, R.; Liljeroth, P. *Nat. Commun.* **2015**, *6*, 10177−10184.

(8) Ruffieux, P.; Cai, J.; Plumb, N. C.; Patthey, L.; Prezzi, D.; Ferretti, A.; Molinari, E.; Feng, X.; Mullen, K.; Pignedoli, C. A.; Fasel, R. *ACS Nano* **2012**, *6*, 6930−6935.

(9) Ruffieux, P.; Wang, S.; Yang, B.; Sanchez-Sanchez, C.; Liu, J.; Dienel, T.; Talirz, L.; Shinde, P.; Pignedoli, C. A.; Passerone, D.; Dumslaff, T.; Feng, X.; Mullen, K.; Fasel, R. *Nature* **2016**, *531*, 489−492.

(10) Nakada, K.; Fujita, M.; Dresselhaus, G.; Dresselhaus, M. S. *Phys. Rev. B: Condens. Matter Mater. Phys.* **1996**, *54*, 17954−17961.

(11) Liu, J.; Li, B.; Tan, Y.; Giannokopoulos, A.; Sanchez-Sanchez, C.; Beljonne, D.; Ruffieux, P.; Fasel, R.; Feng, X.; Mullen, K. *J. Am. Chem. Soc.* **2015**, *137*, 6097−6103.

(12) Cai, J.; Ruffieux, R.; Jaafar, R.; Bieri, M.; Braun, T.; Blankenburg, S.; Muoth, M.; Seitsonen, A.; Saleh, M.; Feng, X.; Mullen, K.; Fasel, R. *Nature* **2010**, *466*, 470−473.

(13) Han, P.; Akagi, K.; Canova, F. F.; Mutoh, H.; Shiraki, S.; Iwaya, K.; Weiss, P. S.; Asao, K.; Hitosugi, R. *ACS Nano* **2014**, *8*, 9181−9187.

(14) Marangoni, T.; Haberer, D.; Rizzo, D. J.; Cloke, R. R.; Fischer, F. R. *Chem. - Eur. J.* **2016**, *22*, 13037−13040.

(15) Bronner, C.; Stremlau, S.; Gille, M.; Brausse, F.; Haase, A.; Hecht, S.; Tegeder, P. *Angew. Chem., Int. Ed.* **2013**, *52*, 4422−4425.

DOI: 10.1021/jacs.7b11886
J. Am. Chem. Soc. 2018, 140, 807−813

(16) Cai, J.; Pignedoli, C. A.; Talirz, L.; Ruffieux, P.; Sode, H.; Liang, L.; Meunier, V.; Berger, R.; Li, R.; Feng, X.; Mullen, K.; Fasel, R. *Nat. Nanotechnol.* **2014**, *9*, 896−900.
(17) Zhang, Y.; Zhang, Y.; Li, G.; Lu, J.; Lin, X.; Du, S.; Berger, R.; Feng, X.; Mullen, K.; Gao, H.-J. *Appl. Phys. Lett.* **2014**, *105*, 023101.
(18) Cloke, R.; Marangoni, T.; Nguyen, G. D.; Joshi, T.; Rizzo, D. J.; Bronner, C.; Cao, T.; Louie, S. G.; Crommie, M. F.; Fischer, F. R. *J. Am. Chem. Soc.* **2015**, *137*, 8872−8875.
(19) Nguyen, G. D.; Toma, F. M.; Cao, T.; Pedramrazi, Z.; Chen, C.; Rizzo, D. J.; Joshi, T.; Bronner, C.; Chen, Y.; Favaro, M.; Louie, S. G.; Fischer, F. R.; Crommie, M. F. *J. Phys. Chem. C* **2016**, *120*, 2684−1687.
(20) Talirz, L.; Ruffieux, P.; Fasel, R. *Adv. Mater.* **2016**, *28*, 6222−6231.
(21) Llinas, J.; Fairbrother, A.; Barin, G.; Shi, W.; Lee, K.; Wu, S.; Choi, B. Y.; Braganza, R.; Lear, J.; Kau, N.; Choi, W.; Chen, C.; Pedramrazi, Z.; Dumslaff, T.; Narita, A.; Feng, X.; Müllen, K.; Fischer, F.; Zettl, A.; Ruffieux, P.; Yablonovitch, E.; Crommie, M.; Fasel, R.; Bokor, J. *Nat. Commun.* **2017**, *8*, 633.
(22) Bennet, P. B.; Pedramrazi, Z.; Madani, A.; Chen, Y.-C.; de Oteyza, D. G.; Chen, C.; Fischer, F. R.; Crommie, M. F.; Bokor. *Appl. Phys. Lett.* **2013**, *103*, 253114.
(23) Li, X.; Wang, X.; Zhang, L.; Lee, S.; Dai, H. *Science* **2008**, *319*, 1229−1232.
(24) Narita, A.; Verhbitskiy, I. A.; Frederickx, W.; Mali, K. S.; Jensen, S. A.; Hansen, M. R.; Bonn, M.; De Feyter, S.; Casiraghi, C.; Feng, X.; Mullen, K. *ACS Nano* **2014**, *8*, 11622−11630.
(25) Deniz, O.; Sanchez-Sanchez, C.; Dumslaff, T.; Feng, X.; Narita, A.; Mullen, K.; Kharche, N.; Meunier, V.; Fasel, R.; Ruffieux, P. *Nano Lett.* **2017**, *17*, 2197−2203.
(26) Wang, S.; Kharche, N.; Girao, E. C.; Feng, X.; Mullen, K.; Meunier, V.; Fasel, R.; Ruffieux, P. *Nano Lett.* **2017**, *17*, 4277−4283.
(27) Kawai, S.; Saito, S.; Osumi, S.; Yamaguchi, S.; Foster, A. S.; Spijker, P.; Meyer, E. *Nat. Commun.* **2015**, *6*, 8098.
(28) Carbonell-Sanroma, E.; Hieulle, J.; Vilas-Varela, M.; Brandimarte, P.; Iraola, M.; Barragan, A.; Li, J.; Abadia, M.; Corso, M.; Sanchez-Portal, D.; Pena, D.; Pascual, J. I. *ACS Nano* **2017**, *11*, 7355−7361.
(29) Linden, S.; Zhong, D.; Timmer, A.; Aghdassi, N.; Franke, J. H.; Zhang, H.; Feng, X.; Mullen, K.; Fuchs, H.; Chi, L.; Zacharias, H. *Phys. Rev. Lett.* **2012**, *108*, 216801.
(30) Vo, T. H.; Perera, G. E.; Shekhirev, M.; Pour, M. M.; Kunkel, D. A.; Lu, H.; Gruverman, A.; Sutter, E.; Cotlet, M.; Nykypanchuk, D.; Zahl, P.; Enders, A.; Sinitskii, A.; Sutter, P. *Nano Lett.* **2015**, *15*, 5770−5777.
(31) Gross, L.; Mohn, F.; Moll, N.; Liljeroth, P.; Meyer, G. *Science* **2009**, *325*, 1110−1114.
(32) Sun, Z.; Boneschanscher, M. P.; Swart, I.; Vanmaekelbergh, D.; Liljeroth, P. *Phys. Rev. Lett.* **2011**, *106*, 046104−046108.
(33) Nguyen, G. D.; Tsai, H.-Z.; Omrani, A. A.; Marangoni, T.; Wu, M.; Rizzo, D. J.; Rodgers, G.; Cloke, R. R.; Durr, R. A.; Sakai, Y.; Liou, F.; Aikawa, A. S.; Chelikowsky, J. R.; Louie, S. G.; Fischer, F. R.; Crommie, M. F. *Nat. Nanotechnol.* **2017**, *12*, 1077−1082.
(34) Giannozzi, P.; Baroni, S.; Bonini, N.; Calandra, M.; Car, R.; Cavazzoni, C.; Ceresoli, D.; Chiarotti, G. L.; Cococcioni, M.; Dabo, I.; Corso, A. D.; de Gironcoli, S.; Faabris, S.; Fratesi, G.; Gebauer, R.; Gerstman, U.; Gougoussis, C.; Kokalj, A.; Lazzeri, Am.; Martin-Samos, L.; Marzari, N.; Mauri, F.; Mazzarello, R.; Paolini, S.; Pasquarello, A.; Paulatto, L.; Sbraccia, C.; Scandolo, S.; Sclauzer, G.; Seitsonnen, A. P.; Smogunov, A.; Umari, P.; Wentzcovitch, R. M. *J. Phys.: Condens. Matter* **2009**, *21*, 395502.
(35) Hybertsen, M. S.; Louie, S. G. *Phys. Rev. B: Condens. Matter Mater. Phys.* **1986**, *34*, 5390.
(36) Chen, Y.-C.; Cao, T.; Chen, C.; Pedramrazi, Z.; Haberer, D.; de Oteyza, D. G.; Fischer, F. R.; Louie, S. G. *Nat. Nanotechnol.* **2015**, *10*, 156.
(37) Hartwigsen, C.; Goedecker, S.; Hutter, J. *Phys. Rev. B: Condens. Matter Mater. Phys.* **1998**, *58*, 3641.
(38) Giessibl, F. J. *Appl. Phys. Lett.* **1999**, *73*, 3956.
(39) Horcas, I.; Fernandez, R.; et al. *Rev. Sci. Instrum.* **2007**, *78*, 013705.
(40) Vanderbilt, D. *Phys. Rev. B: Condens. Matter Mater. Phys.* **1990**, *41*, 7892.

DOI: 10.1021/jacs.7b11886
J. Am. Chem. Soc. 2018, 140, 807−813